University of Reading

Retrieval of sea surface temperature from HY-1B COCTS

Article

Accepted Version

Liu, M., Merchant, C. J. ORCID: https://orcid.org/0000-0003-4687-9850, Embury, O. ORCID: https://orcid.org/0000-0002-1661-7828, Liu, J., Song, Q. and Guan, L. (2022) Retrieval of sea surface temperature from HY-1B COCTS. IEEE Transactions on Geoscience and Remote Sensing, 60. 5002913. ISSN 0196-2892 doi: https://doi.org/10.1109/TGRS.2022.3190444 Available at https://centaur.reading.ac.uk/106451/

It is advisable to refer to the publisher's version if you intend to cite from the work. See Guidance on citing.
Published version at: https://ieeexplore.ieee.org/document/9826829
To link to this article DOI: http://dx.doi.org/10.1109/TGRS.2022.3190444

Publisher: IEEE Geoscience and Remote Sensing Society

All outputs in CentAUR are protected by Intellectual Property Rights law, including copyright law. Copyright and IPR is retained by the creators or other copyright holders. Terms and conditions for use of this material are defined in the End User Agreement.

www.reading.ac.uk/centaur

University of Reading

CentAUR

Central Archive at the University of Reading

Reading's research outputs online

This article has been accepted for publication in IEEE Transactions on Geoscience and Remote Sensing. This is the author's version which has not been fully edited and content may change prior to final publication. Citation information: DOI 10.1109/TGRS.2022.3190444

Retrieval of Sea Surface Temperature from HY-1B COCTS

Mingkun Liu, *Member, IEEE*, Christopher J. Merchant, Owen Embury, Jianqiang Liu, Qingjun Song, Lei Guan, *Member, IEEE*

***Abstract*— The Chinese Ocean Color and Temperature Scanner (COCTS) on board HY-1 series satellites has two thermal infrared channels with the spectrum range of 10.30-11.40 μm and 11.40-12.50 μm for sea surface temperature (SST) observations. To reprocess the Haiyang-1B (HY-1B) COCTS SST, the Bayesian cloud detection and optimal estimation (OE) SST retrieval were applied to COCTS data in this study. The Bayesian cloud detection algorithm that has been developed is based on the Bayes' theorem and uses simulation of COCTS observations. The MODerate resolution atmospheric TRANsmission (MODTRAN) model was used for simulation of COCTS brightness temperatures. SSTs were retrieved from COCTS by OE from 2009 to 2011 in the northwest Pacific. Comparison of COCTS OE SST with in situ SST showed that the COCTS SSTs are cooler than buoy measurements by −0.23 ºC on average, and the standard deviation (SD) of differences was 0.51 ºC. A large component of the mean difference is attributable to the cool skin effect at the ocean surface (typically −0.15 to −0.2 ºC), the remainder being attributable to simulation and calibration biases. The mean difference of COCTS OE SST with matched skin temperatures from the Advanced Along Track Scanning Radiometer (AATSR) is closer to zero, being −0.09 ºC, with a SD of 0.49 ºC. These validation results of COCTS OE SST demonstrate that Bayesian cloud detection and OE SST retrieval algorithm work well for improving COCTS SST accuracy, and show the potential of these methods to help develop SST products for operational HY-1 satellites, HY-1C and HY-1D.**

***Index Terms*— Bayesian cloud detection, Chinese Ocean Color and Temperature Scanner (COCTS), Haiyang-1B (HY-1B), sea surface temperature (SST), optimal estimation (OE)**

I. Introduction

SEA Surface Temperature (SST) is a geophysical parameter crucial to ocean processes and climate change. Satellite observations of SST include infrared and microwave measurements. The accuracy requirement for SST observations is relatively stringent. For numerical weather prediction (NWP), fishery studies, etc., the requirement for SST accuracy is around 0.5 K with high spatial resolution (0.5-10 km) [1]. For climate applications, SST accuracy in the 0.1-0.3 K range is required [1].

Since observations from the second generation Advanced Very High Resolution Radiometer (AVHRR/2) on board NOAA-7 became available, infrared SST retrieval methods have been developed for nearly 40 years and sensor design has improved, bringing better accuracy of SST retrieved from infrared sensors. We list some SST validation results observed from polar infrared radiometers shown in Table I. The comparisons of AVHRR Pathfinder SST version 5.3 dataset with in situ SST from 1998 to 2011 indicated that there was a cold bias for AVHRR Pathfinder SST in the range of −0.31 K to −0.17 K, and a standard deviation (SD) of 0.39 K to 0.49 K [2]. The MODerate Resolution Imaging Spectroradiometers (MODIS) on the Terra and Aqua satellites have been providing high quality global SST data since 1999 and 2002, respectively. The Collection 5 SST products provided by NASA Ocean Biology Processing Group (OBPG) were compared with buoy SST [3]. For Terra MODIS, the median value of SST difference was −0.145 K, with a corresponding SD of 0.510 K and robust standard deviation (RSD) of 0.380 K. For Aqua MODIS, there was a median value of SST difference of −0.205 K, a SD of 0.509 K, and a RSD of 0.388 K [3]. The comparison results of VIIRS SST provided by NOAA Advanced Clear-Sky Processor for Ocean (ACSPO) with in situ SST indicated the mean difference was 0.0 K with the corresponding SD of 0.466 K and 0.359 K for daytime and nighttime, respectively [4]. European

This work was supported in part by the National Key R&D Program of China, grant number 2018YFB0504900/2018YFB0504904, the National Key R&D Program of China, grant number 2019YFA0607001, the National Natural Science Foundation of China, grant number 42006161, and in part by Natural Science Foundation of Shandong, grant number ZR2020QD109. (*Corresponding author: Lei Guan*)

Mingkun Liu is with the College of Marine Technology, Faculty of Information Science and Engineering, Ocean University of China, Qingdao 266100, China, and also with the Laboratory for Regional Oceanography and Numerical Modeling, Qingdao National Laboratory for Marine Science and Technology, Qingdao 266071, China (e-mail: liumingkun@ouc.edu.cn).

Christopher J. Merchant is with the Department of Meteorology, University of Reading, Reading RG6 6ET, UK, and also with the National Centre for Earth Observation, University of Reading, Reading RG6 6ET, UK (e-mail: c.j.merchant@reading.ac.uk).

Owen Embury is with the Department of Meteorology, University of Reading, Reading RG6 6ET, UK, and also with the National Centre for Earth Observation, University of Reading, Reading RG6 6ET, UK (e-mail: o.embury@reading.ac.uk).

Jianqiang Liu is with the National Satellite Ocean Application Service, Ministry of Natural Resources of China, Beijing 100081, China, and also with the Key Laboratory of Space Ocean Remote Sensing and Application, Ministry of Natural Resources of China, Beijing 100081, China (e-mail: jqliu@mail.nsoas.org.cn).

Qingjun Song is with the National Satellite Ocean Application Service, Ministry of Natural Resources of China, Beijing 100081, China, and also with the Key Laboratory of Space Ocean Remote Sensing and Application, Ministry of Natural Resources of China, Beijing 100081, China (e-mail: kingdream@mail.nsoas.org.cn).

Lei Guan is with the College of Marine Technology, Faculty of Information Science and Engineering/Sanya Oceanographic Institution, Ocean University of China, Qingdao 266100/Sanya 572024, China, and with the Laboratory for Regional Oceanography and Numerical Modeling, Qingdao National Laboratory for Marine Science and Technology, Qingdao 266071, China (e-mail: leiguan@ouc.edu.cn).

© 2022 IEEE. Personal use is permitted, but republication/redistribution requires IEEE permission. See https://www.ieee.org/publications/rights/index.html for more information.

This article has been accepted for publication in IEEE Transactions on Geoscience and Remote Sensing. This is the author's version which has not been fully edited and content may change prior to final publication. Citation information: DOI 10.1109/TGRS.2022.3190444

TABLE I
SST VALIDATION RESULTS OBSERVED FROM POLAR INFRARED RADIOMETER

Sensor	Source	Time period	Validation results	Reference
AVHRR	NOAA Pathfinder	From 1998 to 2011	AVHRR minus in situ SST Bias: −0.31~−0.17 K SD: 0.39~0.49 K	[2]
MODIS	NASA OBPG	From 2000 to 2014 (Terra) From 2002 to 2014 (Aqua)	MODIS minus in situ SST Terra MODIS: median: −0.145 K; SD: 0.510 K; RSD: 0.380 K Aqua MODIS: median: −0.205 K; SD: 0.509 K; RSD: 0.388 K	[3]
VIIRS	NOAA ACSPO	From 2012 to 2013	VIIRS minus buoy SST Bias: 0.0 K; SD: 0.466 K (Daytime) Bias: 0.0 K; SD: 0.359 K (Nighttime)	[4]
ATSRs	ESA CCI	From 1992 to 2012	ATSRs minus buoy SST Bias: 0.07 K; RSD: 0.23 K (Daytime) Bias: 0.06 K RSD: 0.23 K (Nighttime)	[6]
SLSTR	EUMETSAT	From 2016 to 2018	SLSTR minus in situ SST Bias: −0.098 K; RSD: 0.296 K SD: 0.565 K	[7]
VIRR	CMA	From 2015 to 2019	VIRR minus in situ SST Bias: −0.21 K; SD: 0.65 K; RSD: 0.58 K (Daytime) Bias: −0.13 K; SD: 0.67 K; RSD: 0.59 K (Nighttime)	[8]

Space Agency (ESA) Climate Change Initiative (CCI) project provided long-term series SST measured from Along Track Scanning Radiometers (ATSRs) [5]. The comparison of ATSRs with buoy SST showed the biases are 0.07 K and 0.06 K for daytime and nighttime, respectively, with the same corresponding RSDs of 0.23 K [6]. The current generation of dual view radiometers, the Sea and Land Surface Temperature Radiometer (SLSTR), also measure SST with high accuracy. The bias was −0.098 K and the RSD was 0.296 K compared with in situ skin temperature [7]. The SST products of Visible and Infrared Radiometer (VIRR) on board Fengyun-3C (FY-3C) satellite were compared with in situ SST and the biases were −0.21 K and −0.23 K with the corresponding RSDs of 0.58 K and 0.59 K for daytime and nighttime, respectively [8].

To derive SST from satellite observed brightness temperature (BT), the cloud detection and clear-sky atmospheric correction are the main steps [9]. The traditional approach for cloud detection is the binary test in a decision tree based on the BT measurements and uniformity test, that was applied in AVHRR, MODIS [3] [10], etc. To address the error detection in cirrus clouds, cloud edges, high-latitude ocean, and SST fronts, the alternative decision tree algorithm based on machine learning is developed, that has been applied in MODIS and VIIRS [11]. Another approach for cloud detection is based on Bayes' theorem, that can determine a probability of clear-sky condition given the satellite observations and prior background information [12]. The Bayesian cloud detection has been used in AATSR series [13], AVHRR [14], the NOAA Geostationary Operational Environmental Satellite (GOES) [15], and Himawari-8 satellite of the Japan Meteorological Agency (JMA) [16]. After the clear-sky observations have been identified, the next step is to retrieve SST. Based on the characteristics of atmospheric radiation transmission in the infrared window, McMillin (1975) proposed that, since the absorption of water vapor in different bands is different, multi-channel observation can be used to remove the influence of water vapor absorption, so as to derive SST [17]. McClain et al. (1985) proposed the Multi-Channel SST (MCSST) algorithm [18] and Walton et al. (1998) improved the retrieval algorithm considering the effect of atmospheric path lengths and the regional dependence of split window BT difference on water vapor, called Non-Linear SST (NLSST) algorithm [1]. The coefficients in MCSST and NLSST algorithm can be derived using two methods. One is based on the atmospheric radiation transfer simulation [19-22], and another one is based on the matchups of in situ SST with measured BTs [4, 18, 23]. Furthermore, Merchant et al. (2008, 2009, 2013) proposed the optimal estimation (OE) SST algorithm, that is the adjustment of the prior SST in the light of the difference between the observed BTs and the simulated BTs assuming the prior SST to be correct [24-26].

Haiyang-1 (HY-1) series satellite is the first-generation of marine-observing satellites of China. HY-1A was launched in May 2002. HY-1B satellite followed in April 2007. HY-1C, launched in September 2018 and HY-1D, launched in June 2020 are the operational satellites of HY-1 series. One of the main payloads on board HY-1 satellites is the Chinese Ocean Color and Temperature Scanner (COCTS). The COCTS is a ten-channel whiskbroom scanner, including eight visible and near infrared channels for ocean color measurements and two thermal infrared channels for observing SST. The spatial resolution of COCTS is 1.1 km at nadir. To reprocess the HY-1B COCTS SST data, inter-calibration of HY-1B COCTS thermal infrared channels with Infrared Atmospheric Sounding

© 2022 IEEE. Personal use is permitted, but republication/redistribution requires IEEE permission. See https://www.ieee.org/publications/rights/index.html for more information.

This article has been accepted for publication in IEEE Transactions on Geoscience and Remote Sensing. This is the author's version which has not been fully edited and content may change prior to final publication. Citation information: DOI 10.1109/TGRS.2022.3190444

Interferometer (IASI) on board MetOp-A satellite was carried out in our previous study [27]. HY-1B COCTS original Level 1B data were provided by the National Satellite Ocean Application Service (NSOAS). After the correction of HY-1B COCTS infrared radiances, the accuracy of BTs from these two channels was improved significantly, and striped noise across scan lines (due to inconsistency between four detectors) was reduced [27].

Based on the re-calibrated BTs, cloud detection and SST retrieval for HY-1B COCTS are investigated in this study. Because of the geographical distribution of the data received from HY-1B at the satellite ground station, we choose the northeast Pacific as the research region in this study. Since striping was not removed completely by inter-calibration, further de-striping of COCTS radiance at the level of image processing is carried out before cloud detection and SST retrieval.

This paper is organized as follows. Section 2 is the de-striping of HY-1B COCTS re-calibrated radiance image. In section 3, we describe the cloud detection of de-striped BT. In Section 4, the OE retrieval algorithm of HY-1B COCTS SST is introduced. Section 5 reports the validation of COCTS OE SST. Conclusions are presented in Section 6.

II. De-striping of HY-1B COCTS infrared radiance

COCTS is a whiskbroom scanner, with four parallel detectors along-track. The different spectral responses of these four parallel detectors caused the sharp striped noise across the scan lines, leading to significant radiometric errors in radiances, which further propagate into retrieved SSTs. Thus, de-striping is one of main steps for improving the SST accuracy of HY-1B COCTS, and better SST gradient estimates. In the inter-calibration study, the COCTS radiance correction coefficients were obtained separately for four detectors. The striped noise in HY-1B COCTS corrected radiance were reduced significantly, but not fully be eliminated, presumably because of the residual error or temporal evolution of the calibration differing between detectors. Therefore, in this study, the further de-striping for HY-1B COCTS corrected radiance is carried out before cloud detection and SST retrieval.

The de-striping method is based on the unidirectional variational model, which has been successfully utilized in MODIS de-striping [28]. We will introduce this de-striping algorithm briefly here. The striping can be assumed to be unidirectional noise as it does not affect the image horizontal gradient. In Bouali and Ignatov (2013), the authors proposed the de-striping can be viewed as an optimization problem based on the minimization of a unidirectional variational model [28]. Fig. 1 and Fig. 2 are regional radiance images of COCTS 11 and 12 μm channel on 11 February 2009, respectively, with Fig. 1 (a) and 2 (a) being the re-calibrated radiance and Fig. 1 (b) and 2 (b) being the de-striped radiance. The line plots indicate radiance variations along track at the location of black lines drawn in each radiance image. The radiance images before de-striping, as well as the fluctuations of the re-calibrated radiance variations, display the residual striping in COCTS re-calibrated radiance data. After de-striping, the striped noise is effectively removed. To demonstrate the high-frequency signal is preserved before and after de-striping, an analysis of the frequency spectrum is carried out. Because the striped noise only exists in the along-track direction, the de-striping should not change the variations in across-track direction. We demonstrate this choosing a region of ocean fronts and compare the spectrum in along-track and across-track directions before and after de-striping. Fig. 3 and 4 are regional radiance images corresponding with power spectrums of HY-1B COCTS 11 and 12 μm channel BT before and after de-striping. The subfigures (a) and (b) are regional radiances before and after de-striping. The subfigures (c) and (d) show the power spectra of the selected scenes, along track and across track respectively, as a function of normalized wavenumber, before and after de-striping. The normalized wavenumber denotes the spatial frequency of stripes. For example, the normalized wavenumber 0.125 means that there exists a stripe per eight scans. To improve visibility, the spectral magnitudes are plotted with a logarithmic scale. There is a broad reduction in power between around 0.125 and 0.5 in normalized wavenumber, suggesting the removal of variability corresponding to cycles between per two scans and per eight scans. For 11 COCTS 11 μm channel, the more marked reductions in power is at wavenumber of 0.5, exactly corresponding to a cycle per two scan line. For COCTS 12 μm channel, the most significant change of spectrum variations along track after de-striping is at wavenumber of 0.5 and 0.25, that is consistent with removing a striping pattern over a cycle per two scan lines and a cycle per four scan lines. In the along scan direction, the spectrum variations almost coincide at all wavenumbers. This indicates that the striping is removed after de-striping, while other non-noise signals are preserved. The following cloud detection and SST retrieval are based on the de-striped radiance.

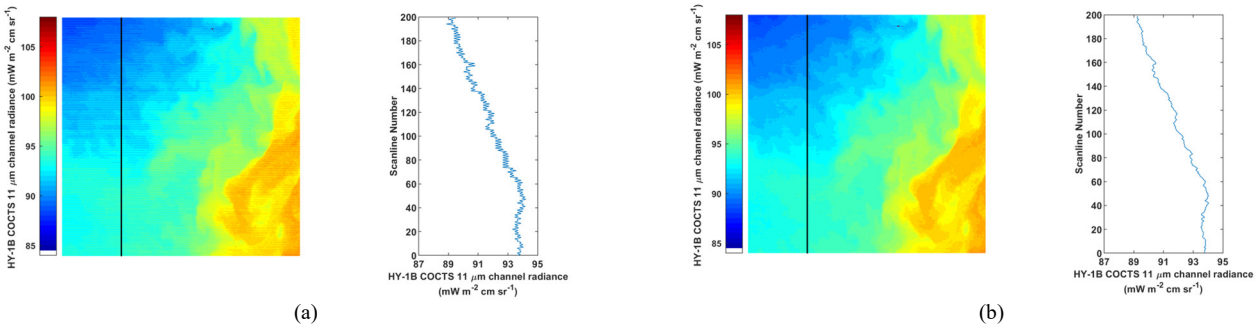

(a) (b)

Fig. 1. Regional radiance images of HY-1B COCTS 11 μm channel on 11 February 2009: (a) before de-striping, (b) after de-striping.

© 2022 IEEE. Personal use is permitted, but republication/redistribution requires IEEE permission. See https://www.ieee.org/publications/rights/index.html for more information.

This article has been accepted for publication in IEEE Transactions on Geoscience and Remote Sensing. This is the author's version which has not been fully edited and content may change prior to final publication. Citation information: DOI 10.1109/TGRS.2022.3190444

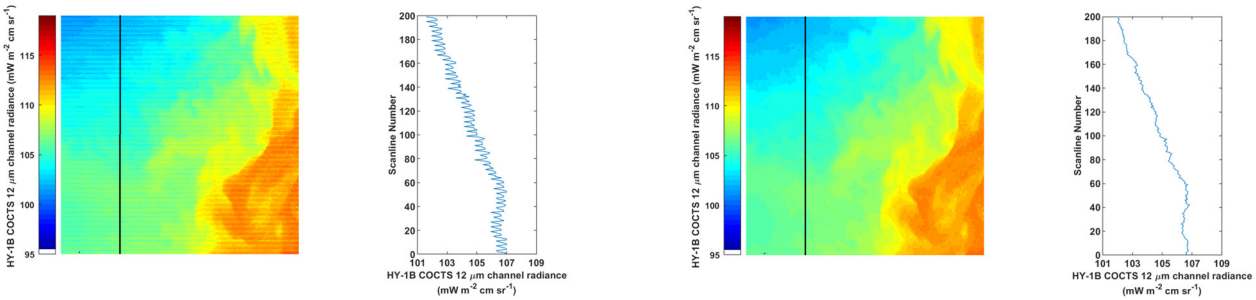

Fig. 2. Regional radiance images of HY-1B COCTS 12 μm channel on 11 February 2009: (a) before de-striping, (b) after de-striping.

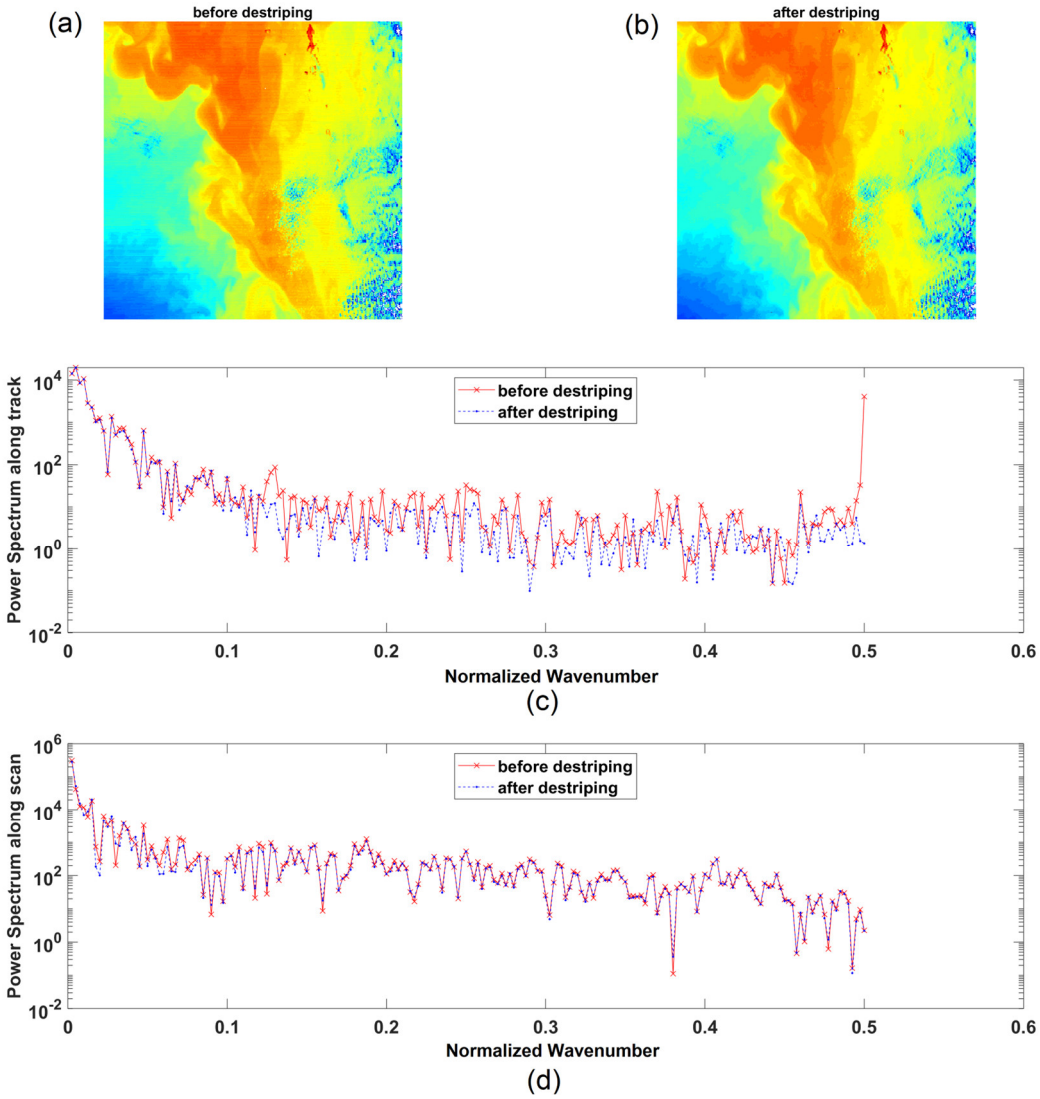

Fig. 3. Regional radiance images of HY-1B COCTS 11 μm channel on 11 February 2009: (a) before de-striping, (b) after de-striping, (c) power spectra along track, and (d) along scan.

© 2022 IEEE. Personal use is permitted, but republication/redistribution requires IEEE permission. See https://www.ieee.org/publications/rights/index.html for more information.

This article has been accepted for publication in IEEE Transactions on Geoscience and Remote Sensing. This is the author's version which has not been fully edited and content may change prior to final publication. Citation information: DOI 10.1109/TGRS.2022.3190444

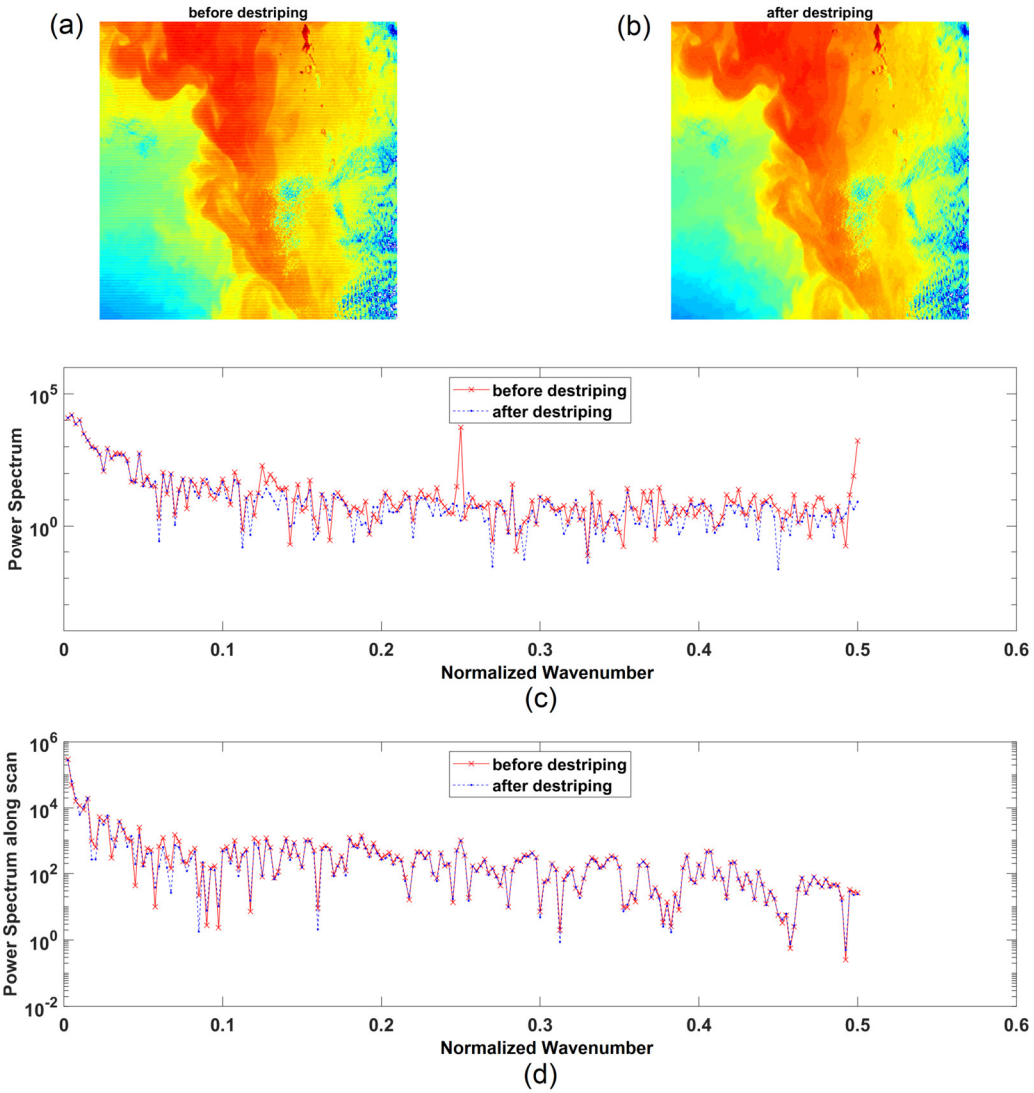

Fig. 4. Regional radiance images of HY-1B COCTS 12 μm channel on 11 February 2009: (a) before de-striping, (b) after de-striping, (c) power spectra along track, and (d) along scan.

III. Bayesian Cloud Detection

The cloud detection of infrared instruments is a pre-processing step for SST retrieval. In this paper, a Bayesian approach is utilized for cloud detection of COCTS infrared BTs. Bayesian cloud detection is based on Bayes' theorem, determining a clear-sky probability given the satellite observations and prior background information. Merchant et al. (2008) described a methodology of Bayesian cloud detection in detail [12]. In this paper, we focus on the application to COCTS. Thus, the general concept is introduced briefly here, with a detailed description of specific application to COCTS.

The probability of clear sky is calculated using Bayes' theorem, given the satellite observations and the background information. The length scale of clear-sky probability variation (~1 km) is much finer than the length scale of variation in the atmospheric terms in the background state (~100 km). Thus, on pixel-to-pixel scales, the background state is independent of clear-sky probability. Based on this assumption, the expression for probability of clear sky can be shown as:

$$P(c|\boldsymbol{y}^o,\boldsymbol{x}^b)=\left[1+\frac{P(\bar{c})P(\boldsymbol{y}^o|\boldsymbol{x}^b,\bar{c})}{P(c)P(\boldsymbol{y}^o|\boldsymbol{x}^b,c)}\right]^{-1} \quad (1)$$

where P represents a probability or probability density function (PDF), c indicates clear sky, $\boldsymbol{y}$ is the satellite observation, $\boldsymbol{x}$ is the state vector, superscript o represents 'observed', and superscript b represents 'background' [12]. The equation (1) shows that in order to estimate the $P(c|\boldsymbol{y}^o,\boldsymbol{x}^b)$, we need to calculate the prior estimate of the clear sky $P(c)$, and the probabilities of the satellite observations given the background state under clear and cloudy conditions, $P(\boldsymbol{y}^o|\boldsymbol{x}^b,c)$ and $P(\boldsymbol{y}^o|\boldsymbol{x}^b,\bar{c})$, respectively. For COCTS cloud detection, the observation vector $\boldsymbol{y}^o$ includes the observed BTs of COCTS 11 μm and 12 μm channels and the local SD (LSD) of the BTs in a 3 by 3 box ($LSD_{3\times3}$) centered on the current pixel. Because of the unstable calibration of COCTS reflectance channels, the reflectance channels are not utilized for the cloud detection here. The background state vector $\boldsymbol{x}^b$ consists of the background SST and total column water vapor (TCWV) from ECMWF ERA-Interim NWP data [29-30], which has a spatial resolution

© 2022 IEEE. Personal use is permitted, but republication/redistribution requires IEEE permission. See https://www.ieee.org/publications/rights/index.html for more information.

This article has been accepted for publication in IEEE Transactions on Geoscience and Remote Sensing. This is the author's version which has not been fully edited and content may change prior to final publication. Citation information: DOI 10.1109/TGRS.2022.3190444

around 0.7°×0.7° in the northwest Pacific. The background observation vector $\boldsymbol{y}^b$ indicates the expected observation vector given the background state $\boldsymbol{x}^b$. This is simulated using MODerate resolution atmospheric TRANsmission (MODTRAN) 5.3.3 to compute top-of-atmospheric BT, given the atmospheric profiles, surface parameters, and the spectral response functions (SRFs) of COCTS. The cloud detection of COCTS is processed pixel by pixel. For COCTS pixels, the flag mask is set to 'invalid' under the conditions of land, being outside the study area, or having satellite zenith angle larger than 50°. In addition, the pixel is considered obviously cloudy if the 11 μm BT is less than 260 K.

The observation vector, $\boldsymbol{y}^o$, consists of spectral (BT) and textural (LSD) components denoted as $\boldsymbol{y}_s^o$ and $\boldsymbol{y}_t^o$ respectively, and these two parts are independent, thus the $P(\boldsymbol{y}^o|\boldsymbol{x}^b)$ can be written as [12]:

$$P(\boldsymbol{y}^o|\boldsymbol{x}^b) = P(\boldsymbol{y}_s^o|\boldsymbol{x}^b) \times P(\boldsymbol{y}_t^o|\boldsymbol{x}^b) \quad (2)$$

It is assumed that BTs in the case of clear-sky has a Gaussian distribution, therefore the $P(\boldsymbol{y}_s^o|\boldsymbol{x}^b, c)$ can be calculated using the joint PDF of Gaussian distribution [12]. However, for cloudy sky, the BT distribution is not the Gaussian, thus the $P(\boldsymbol{y}_s^o|\boldsymbol{x}^b, \bar{c})$ must be determined using empirical cloudy PDF look-up tables (LUTs) [12]. For the texture component, both $P(\boldsymbol{y}_t^o|\boldsymbol{x}^b, c)$ and $P(\boldsymbol{y}_t^o|\boldsymbol{x}^b, \bar{c})$ need to be determined using empirical PDF LUTs. ESA CCI provided PDFs using the entire ATSR time series of observations [31]. It's not feasible to generate the PDF LUT using COCTS observations here because the COCTS data volume is not enough. Because the channel characteristics of COCTS is different compared with ATSRs, such as the SRFs and noise levels for 11 and 12 μm channels, the PDF LUTs based on ATSRs observations need to be adjusted for COCTS cloud detection.

For texture part, the ATSRs PDF LUT provided the PDF under different 11 μm $LSD_{3\times3}$ values and satellite zenith angles on day/night. Because the noise of COCTS is larger than ATSRs, thus using ATSRs texture LUT directly for COCTS texture PDF calculation is not reasonable. We convolved the PDF distribution of COCTS noise with AATSR clear/cloudy texture PDF to obtain texture PDF applicable to COCTS cloud detection, shown as Fig. 5 (a) and (b) where blue curve indicating as AATSR clear/cloudy PDF and black curve representing as COCTS clear/cloudy PDF at nadir direction. The computational details for the texture PDF for COCTS cloud detection are introduced in the appendix.

For spectral part, the two channel AATSR cloudy PDF LUT has five dimensions, including "11 μm BT minus NWP SST", "11 μm BT minus 12 μm BT", "NWP SST", "path length" and "day/night". Given the different SRFs of COCTS and AATSR, BT adjustments are required to use AATSR PDF with COCTS. We choose IASI as the "shift bridge" owing to its hyperspectral nature and high-quality measurements. The SRFs of COCTS and AATSR are convolved with IASI spectral radiance to obtain the IASI-convolved BTs corresponding to COCTS and AATSR channel specification, respectively. The COCTS BT shift is generated by the linear regression based on the IASI-convolved BTs.

In this paper, we designate pixels with $P(c|\boldsymbol{y}^o, \boldsymbol{x}^b)$ larger than 0.9 as clear sky [12]. Fig. 6 (a) and (b) are the COCTS 11μm BTs on 7 May 2011 before and after cloud detection respectively, where gray indicates invalid regions (such as land, beyond the study area, or satellite zenith angle larger than 50°) and white represents cloudy sky. The figures show that the cloudy detection is giving plausible results, and we will also validate the cloud mask performance using the retrieved SST evaluation results in the following part.

IV. Optimal Estimation SST Retrieval

A. Introduction to the OE SST retrieval algorithm

In this paper, the COCTS SSTs were retrieved by OE algorithm from 2009 to 2011 in the northwest Pacific. OE is the adjustment of the prior SST in the light of the difference between the observed BTs and the BTs that are simulated assuming the prior SST to be correct [24-26]. For OE SST retrieval, SST is estimated through a weighted combination of the prior SST and TCWV, and the difference between the observations and the simulated BTs given the prior field. The covariance matrix of prior and satellite observation, as well as the prior information are also necessary for SST estimation. The

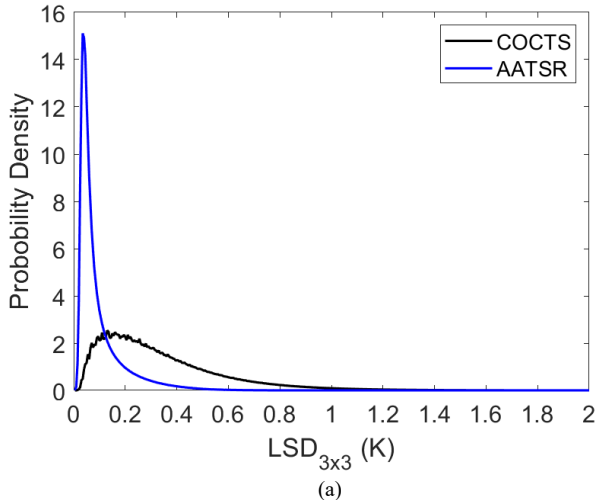

(a)

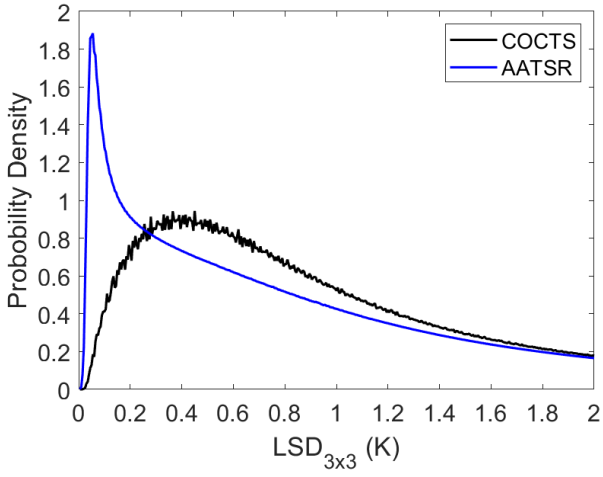

(b)

Fig. 5. The texture PDF of COCTS (black curve) and AATSR (blue curve) in (a) clear and (b) cloudy sky.

© 2022 IEEE. Personal use is permitted, but republication/redistribution requires IEEE permission. See https://www.ieee.org/publications/rights/index.html for more information.

This article has been accepted for publication in IEEE Transactions on Geoscience and Remote Sensing. This is the author's version which has not been fully edited and content may change prior to final publication. Citation information: DOI 10.1109/TGRS.2022.3190444

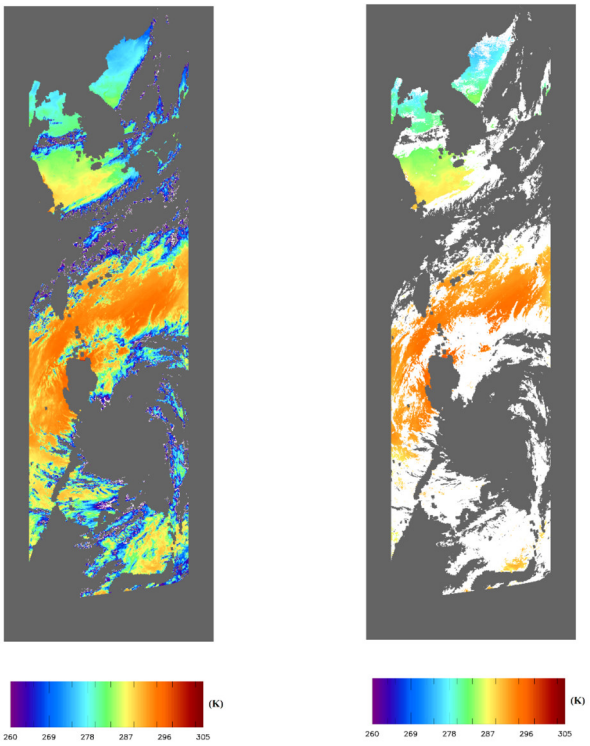

(a) (b)

Fig. 6. COCTS 11 μm scene BT on 7 May, 2011: (a) before and (b) after cloud detection

OE SST can be obtained through the following equation (3) [24-26],

$$\hat{\mathbf{x}} = \mathbf{x_a} + (\mathbf{K}^{\mathrm{T}}\mathbf{S}_{\varepsilon}^{-1}\mathbf{K} + \mathbf{S}_{\mathrm{a}}^{-1})^{-1}\mathbf{K}^{\mathrm{T}}\mathbf{S}_{\varepsilon}^{-1}\left(\mathbf{y}^{\mathrm{o}} - \mathbf{F}(\mathbf{x}_{\mathrm{a}})\right) \quad (3)$$

where $\boldsymbol{x}_a$ indicating the prior state, including the prior SST and TCWV from ECMWF ERA-Interim NWP data [29-30], and $\boldsymbol{y}^o$ representing the observed BTs from 11 μm and 12 μm channels. $\boldsymbol{F}(\boldsymbol{x}_a)$ is the MODTRAN simulated BTs from 11 μm and 12 μm channels given the prior state. $\boldsymbol{K}$ is the Jacobian matrix, expressing the partial derivatives of the BT variation with respect to prior state vector. $\boldsymbol{S}_\varepsilon$ is the error covariance of the observations relative to the forward model, including the uncertainty of the atmospheric radiative model and the sensor noise. The model uncertainty is set as 0.2 K according to the comparison of MODTRAN simulated BT with line-by-line model [32]. The sensor noise we set is 0.2 K, that is the NEDT of COCTS infrared channels (https://directory.eoportal.org/web/eoportal/satellite-missions /h/hy-1b). The $\boldsymbol{S}_a$ is the prior error covariance, including the uncertainty of prior TCWV (e_{wa}) and the uncertainty of prior SST (e_{SSTa}). The uncertainty of TCWV is determined using the proposed parameterization in Merchant et al. (2013), that is expressed as the following equation (4) [26],

$$\mathrm{e_{wa}} = 0.5 \times \mathrm{TCWV} \times \left(0.1 + \frac{75 - \mathrm{TCWV}}{150}\right) [\mathrm{TCWV\ in\ kg/m^2}] \quad (4)$$

The determination of e_{SSTa} affect the OE SST accuracy and spatial precision, thus playing the important role on OE SST retrieval. In the following part, we mainly focus on the e_{SSTa} determination of COCTS OE SST retrieval case.

B. The determination of prior SST uncertainty

The e_{SSTa} affects the OE SST accuracy and spatial precision directly. The spatial resolution of prior SST is around 70 km. If e_{SSTa} is underestimated, this means that the OE SST relies more on the large-scale prior SST, leading to the decreased spatial fidelity of the observed SST fields at the full satellite resolution. Another way to express this is that the SST sensitivity in this case is low, which leads to underestimation of features such as the change in SST over an ocean front [33]. On the other hand, overestimated e_{SSTa} means a sub-optimal amount of conditioning of the retrieval by the prior information, causing larger OE SST uncertainty from greater propagation of errors in the satellite observations and simulated BTs. This increased uncertainty is present on a range of spatial scales, including higher pixel-to-pixel 'noise' in the retrieved SST. The choice of e_{SSTa} needs to be determined considering both SST uncertainty and spatial fidelity. We compare the prior SST with iQuam buoy SST based on the matchups between COCTS and iQuam buoy SST. For matching, the temporal window is set as 1 hour and the spatial window is 0.01º×0.01º. The comparison results show that the mean difference of prior SST minus buoy SST is −0.12 ºC, with the corresponding standard deviation of 0.50 ºC. Minimizing the overall error variance is not the only choice for how to optimise the retrieval result [26], and locally (near fronts or when there is strong diurnal warming) such a general value may underestimate the prior SST uncertainty. Thus, we try to set e_{SSTa} equal to 0.1 K, 0.5 K, 1.2 K, 2.0 K, 3.0 K, and 5.0 K, to explore the OE SST uncertainty and spatial fidelity obtained.

The accuracy of COCTS OE SST using different e_{SSTa} values is explored by comparing COCTS OE SST with matched iQuam buoy SST. For matching, the temporal window is set as 1 hour and the spatial window is 0.01º×0.01º. Table II shows the comparison results of COCTS OE SST minus buoy SST difference. When the e_{SSTa} is set as 0.1 K, meaning that the COCTS retrieved SST almost entirely rely on the prior state, the mean difference between COCTS OE SST and buoy is −0.12 ºC, with the corresponding SD of 0.49 ºC. With the increasing of e_{SSTa}, the absolute value of the negative bias becomes larger, and the SD increase. When the e_{SSTa} is set as 5.0 K, the COCTS OE SST almost entirely rely on the satellite observations under this situation, with the bias being −0.53 ºC and the SD being 1.32 ºC.

Next, the spatial precision of COCTS OE SST image is analyzed. We choose a region in SST fronts for the spatial precision analysis. Fig. 7 (a) and (b) are the regional prior SST and the COCTS 11 μm BT, respectively. The left panels of Fig. 8 (a)-(f) are the regional COCTS OE SSTs when e_{SSTa} is set as 0.1 K, 0.5 K, 1.2 K, 2.0 K, 3.0 K, and 5.0 K, respectively. The patterns in Fig. 8 (a) and Fig. 7 (a) are similar at large scales, while the satellite image shows details of finer-scale feature. With the increasing e_{SSTa}, the details of the SST features become clear, indicating the improvement of spatial fidelity. The appearance of finer detail in OE SST is comparable to that in the 11 μm BTs when $e_{SSTa} \geq 1.2$ K. To compare the spatial precision quantitatively, the histograms of the LSD in 11×11 boxes ($\mathrm{LSD_{11\times11}}$) in different regional images are plotted, shown as the right panels in Fig. 8 (a)-(f). The blue curves, red curves and black curves represent $\mathrm{LSD_{11\times11}}$ histograms of prior SST, COCTS OE SST and 11 μm BT, respectively in Fig. 8,

© 2022 IEEE. Personal use is permitted, but republication/redistribution requires IEEE permission. See https://www.ieee.org/publications/rights/index.html for more information.

This article has been accepted for publication in IEEE Transactions on Geoscience and Remote Sensing. This is the author's version which has not been fully edited and content may change prior to final publication. Citation information: DOI 10.1109/TGRS.2022.3190444

where (a)-(f) indicate that e_{SSTa} is set as 0.1 K, 0.5 K, 1.2 K, 2.0 K, 3.0 K, and 5.0K, respectively. For prior SST, the $LSD_{11\times11}$ is distributed over the range from 0 K to 0.15 K, indicating that the spatial precision is relatively low. The histogram of OE SST is almost superposed with that of the prior SST when e_{SSTa} is set as 0.1 K. With the increasing e_{SSTa}, the peak of the $LSD_{11\times11}$ histogram for OE SST moves right, in response to a combination of increased sensitivity to surface variability and increasing noise propagation. When the e_{SSTa} increases to 1.2 K, the $LSD_{11\times11}$ histograms for OE SST coincide with that for 11 μm BT, indicating that the feature detail for OE SST has been reached to close level compared to 11 μm BT. When e_{SSTa} is set as 2 K, 3K, or 5 K, the histogram for OE SST moves right relative to that for 11 μm BT. In addition, we also calculated the SST sensitivities by choosing the 112 clearest scenes. The mean SST sensitivity increases with the increasing e_{SSTa}. When e_{SSTa} is set as 1.2 K, the mean SST sensitivity is 41%. It's necessary to find the trade-off among the expected retrieval accuracy, the SST sensitivity and retaining spatial fidelity. There is a trade-off between retaining spatial detail and suppressing SST noise. In conclusion, considering both the SST accuracy and spatial fidelity, we set e_{SSTa} as 1.2 K for COCTS OE SST retrieval in this research.

TABLE II
THE COMPARISON RESULTS OF COCTS OE SST MINUS BUOY SST DIFFERENCE WITH DIFFERENT e_{SSTa} VALUES

e_{SSTa} (K)	COCTS OE SST minus buoy SST difference	
	bias (°C)	SD (°C)
0.1	−0.12	0.49
0.5	−0.18	0.48
1.2	−0.31	0.58
2.0	−0.42	0.87
3.0	−0.48	1.10
5.0	−0.53	1.32

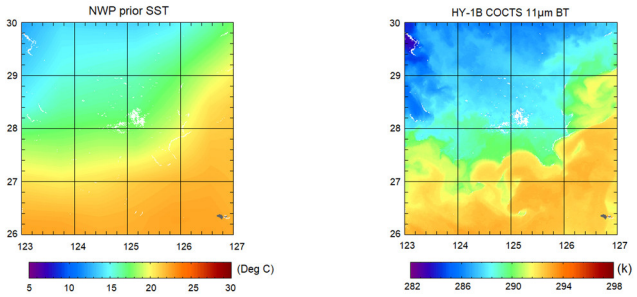

(a) (b)

Fig. 7. Regional (a) prior SST and (b) COCTS 11 μm BT on 22 January 2009.

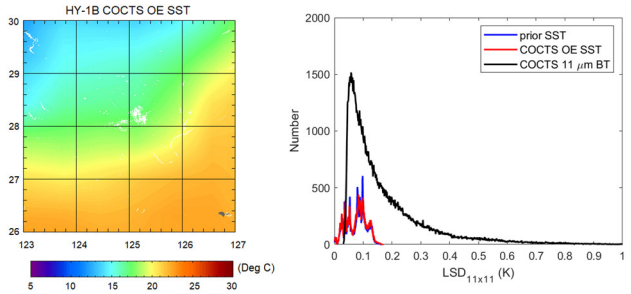

(a) e_{SSTa}=0.1 K

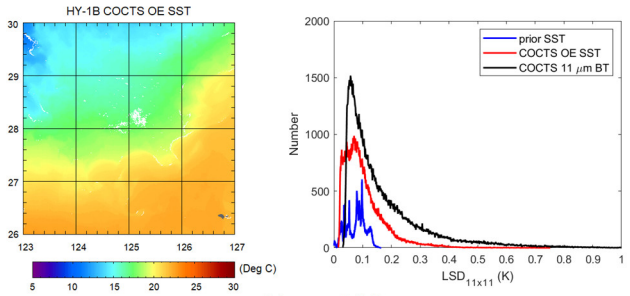

(b) e_{SSTa}=0.5 K

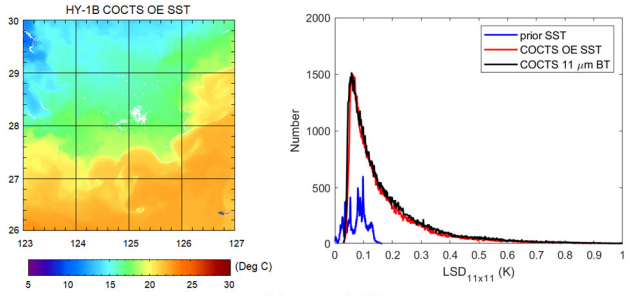

(c) e_{SSTa}=1.2 K

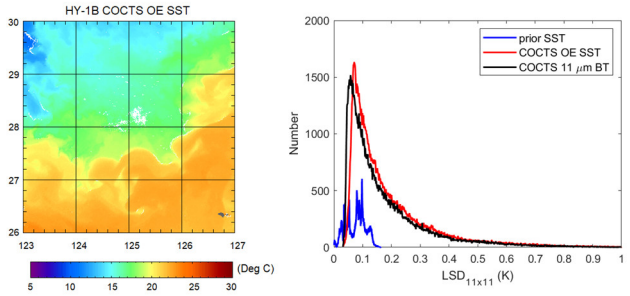

(d) e_{SSTa}=2.0 K

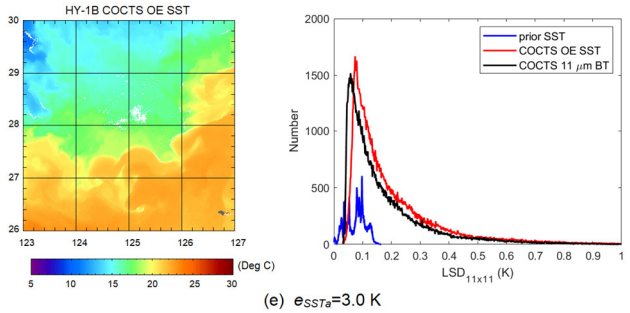

(e) e_{SSTa}=3.0 K

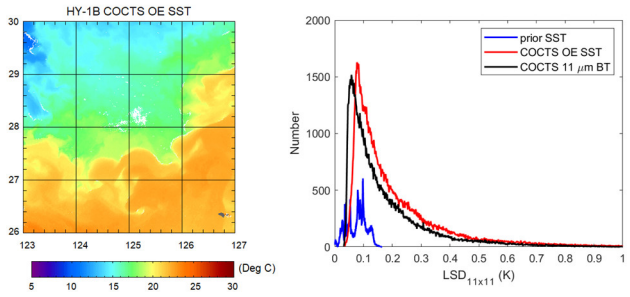

(f) e_{SSTa}=5.0 K

Fig. 8. Regional OE SST and the corresponding $LSD_{11\times11}$ histogram distributions for regional OE SST, prior SST and 11 μm BT in different e_{SSTa} cases: (a) e_{SSTa}=0.1 K; (b) e_{SSTa}=0.5 K; (c) e_{SSTa}=1.2 K; (d) e_{SSTa}=2.0 K; (e) e_{SSTa}=3.0 K; (f) e_{SSTa}=5.0 K.

© 2022 IEEE. Personal use is permitted, but republication/redistribution requires IEEE permission. See https://www.ieee.org/publications/rights/index.html for more information.

This article has been accepted for publication in IEEE Transactions on Geoscience and Remote Sensing. This is the author's version which has not been fully edited and content may change prior to final publication. Citation information: DOI 10.1109/TGRS.2022.3190444

C. *Quality control for OE SST*

Quality flags attached to SST products provide necessary auxiliary information for users. It is convenient for SST users to select data with different quality levels according to different needs. For OE SST retrieval algorithm, the consistency between satellite observations and simulations can be used as an effective criterion to evaluate the SST confidence index [24]. A suitable consistency metric is the chi-squared ($\hat{\chi}^2$), that is readily available in the context of OE [34]. $\hat{\chi}^2$evaluates whether the differences between prior and retrieval are consistent with their expected gaussian distribution, whose covariance S_δ is given by the following equation (5) [34]:

$$\mathbf{S}_\delta = \mathbf{S}_\epsilon(\mathbf{K}\mathbf{S}_a\mathbf{K}^T + \mathbf{S}_\epsilon)^{-1}\mathbf{S}_\epsilon \quad (5)$$

For every retrieved OE SST pixel, there is a corresponding $\hat{\chi}^2$ value, calculated using the equation (6) [34]:

$$\hat{\chi}^2 = \left(\mathbf{K}(\hat{\mathbf{x}} - \mathbf{x}_a) - (\mathbf{y}^o - \mathbf{F}(\mathbf{x}_a))\right)^T (\mathbf{S}_\delta)^{-1} \left(\mathbf{K}(\hat{\mathbf{x}} - \mathbf{x}_a) - (\mathbf{y}^o - \mathbf{F}(\mathbf{x}_a))\right) \quad (6)$$

Fig. 9 is the variations of SST difference between COCTS OE SST and buoy SST against $\hat{\chi}^2$, where the background color indicating the collocation numbers in the $\hat{\chi}^2$ bin of 0.04 and SST difference bin of 0.02 °C. The purple curve represents the SST difference variation, and the black bars indicate the corresponding SDs. With the increasing $\hat{\chi}^2$, the absolute value of the negative biases as well as the SDs become larger, demonstrating that the $\hat{\chi}^2$ is an effective indicator to express the quality level of OE SST. Table III shows the statistics of comparison results between COCTS OE SST and buoy SST. According to the validation results, we set the SST with the $\hat{\chi}^2$ values ranging from 0 to 2 as the high-quality data, and $2 < \hat{\chi}^2 < 5$ is the moderate-quality level. If $\hat{\chi}^2 > 5$, the SST data are considered as low-quality, since the degree of inconsistency indicated by the high $\hat{\chi}^2$ value indicates that the retrieval assumptions are less valid for these data.

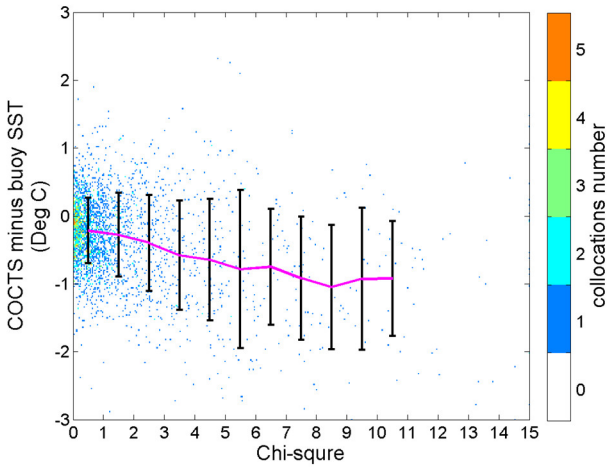

Fig. 9. The variation of COCTS OE SST minus buoy SST difference against Chi-square. The background color indicates the collocation numbers in the $\hat{\chi}^2$ bin of 0.04 and SST difference bin of 0.02 °C. The purple curve represents the SST difference variation, and the black bars indicate the corresponding SDs.

TABLE III
THE COMPARISON RESULTS OF COCTS OE SST WITH BUOY SST IN DIFFERENT $\hat{\chi}^2$ RANGES

χ^2	COCTS OE SST minus buoy SST difference		
	bias（°C）	SD（°C）	collocation percentage（%）
$0<\chi^2<1$	−0.22	0.48	60.62
$1<\chi^2<2$	−0.28	0.61	16.40
$2<\chi^2<5$	−0.50	0.78	16.05
$\chi^2>5$	−0.86	1.02	6.93

V. COCTS OE SST VALIDATION

In this research, in situ SST and AATSR CCI SST are used to validate COCTS OE retrieved SST. Here we select the COCTS OE SSTs that are assigned high-quality level for detailed validation.

The in situ SST data used for SST validation is from the in situ SST Quality Monitor System (iQuam), developed by the NOAA Center for Satellite Application and Research (STAR) (https://www.star.nesdis.noaa.gov/socd/sst/iquam/index.html). iQuam SST data are quality-controlled in situ data from the original Global Telecommunication System (GTS) datasets. Considering the reliability and accuracy of the in situ data, only buoy data in best quality level are selected for validation in this paper. The uncertainties using three-way analysis were estimated to be ~0.21 K for drifters and ~0.17 K for tropical moorings, respectively [35]. COCTS OE SSTs are collocated with iQuam buoy measurements. The temporal window of matchups is set as 1 hour and the spatial window is 0.01°×0.01°. The total matchup number is 2433. The mean difference of COCTS OE SST minus buoy SST is −0.23 °C and the SD is 0.51°C. Fig. 10 shows the variation of SST difference against buoy SST. The background color represents the collocation numbers located in buoy SST bin of 0.1°C and SST difference bin of 0.02 °C. The purple line is the variation of mean SST difference in every 2 °C SST bin and the black bars represent the two times uncertainty in the mean. The orange horizontal line at −0.17 °C SST difference represent the cool skin effect [36]. The results of Donlon et al. (2002) showed that in a calm sea with a wind speed of about 6 m/s, the skin temperature was about 0.17°C lower than bulk temperature observed by buoys [36]. Most collocations are located in warm water. In the SST range from 24 °C to 30 °C, the biases are stable around −0.17 °C with the lower uncertainties. In the SST range lower than 20 °C, the mean difference of COCTS minus buoy SST is around −0.35 °C with relatively larger uncertainties. Fig. 11 is the variation of SST difference against TCWV. SST differences are stable in the whole TCWV range within their uncertainties, also not representing dependence on TCWV, indicating that the OE algorithm can effectively eliminate the influence of water vapor. The difference between satellite observation and MODTRAN simulation is one reason causing the cold bias between OE SST and buoy measurements. In addition, the depth difference of infrared sensor measurement with buoy also lead to the SST difference, usually representing that the skin temperature measured by infrared instrument is colder than bulk temperature measured by buoy. The observation depth difference between COCTS and buoy can therefore explain a significant fraction of the −0.23°C discrepancy, suggesting the

© 2022 IEEE. Personal use is permitted, but republication/redistribution requires IEEE permission. See https://www.ieee.org/publications/rights/index.html for more information.

This article has been accepted for publication in IEEE Transactions on Geoscience and Remote Sensing. This is the author's version which has not been fully edited and content may change prior to final publication. Citation information: DOI 10.1109/TGRS.2022.3190444

actual retrieval bias in the COCTS OE SST is less than 0.1°C in magnitude. Systematic errors with buoy data, prior SST and prior WV also contribute to the difference between COCTS OE SST and buoy SST.

AATSR SST is also selected as a reference to validate COCTS OE SST. AATSR L2P SST products are obtained from the SST CCI project of ESA [5]. These AATSR SSTs use a dual-view two-channel retrieval method and have uncertainty around 0.23 ºC [6]. The descending node of AATSR is 10:30 am, that is very close to the descending time of COCTS around 10:30 am±30 min. In addition, SSTs observed by COCTS and AATSR are both skin temperatures with the same measurement depth. We choose 112 scenes of COCTS OE SST to compare with AATSR SSTs. COCTS OE SST and AATSR SST are projected on equal grid map with the spatial resolution of 0.01º×0.01º. The total matchup number is 7264012. The comparison results show that the mean difference of COCTS OE SST minus AATSR SST is −0.09 ºC and the SD is 0.49 ºC. Fig. 12 shows the histograms of COCTS OE SST minus buoy SST difference and COCTS OE SST minus AATSR SST difference. Compared with the statistic results between COCTS and buoy SST difference, the mean difference between COCTS OE SST and AATSR is smaller, and the histogram distribution move right, demonstrating that the main reason of the −0.23 ºC bias between COCTS and buoy is due to the measurement depth difference. And the bias difference between two validation results is 0.14 ºC, that is close to the accepted typical value around −0.17 ºC. In addition, the cold tail is modest in these two histograms, indicating that cloud missing detection is not affecting a large fraction of data.

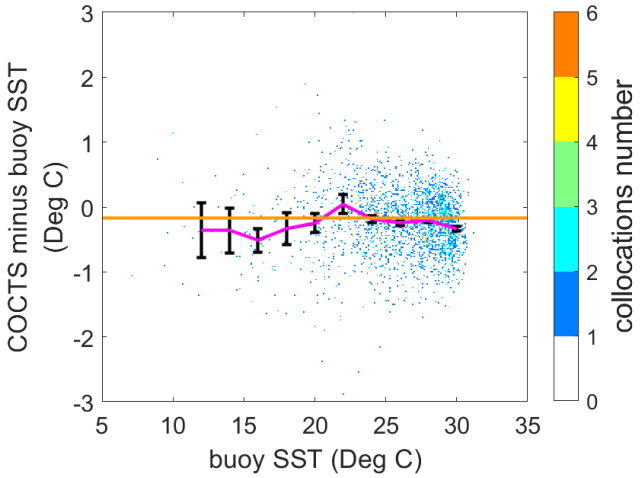

Fig. 10. The variations of COCTS minus buoy SST difference against buoy SST. The background color represents the collocation numbers located in buoy SST bin of 0.1°C and SST difference bin of 0.02 °C. The purple line is the variation of mean SST difference in every 2 °C SST bin and the black bars represent the two times uncertainty in the mean. The orange horizontal line at −0.17 °C SST difference represent the cool skin effect.

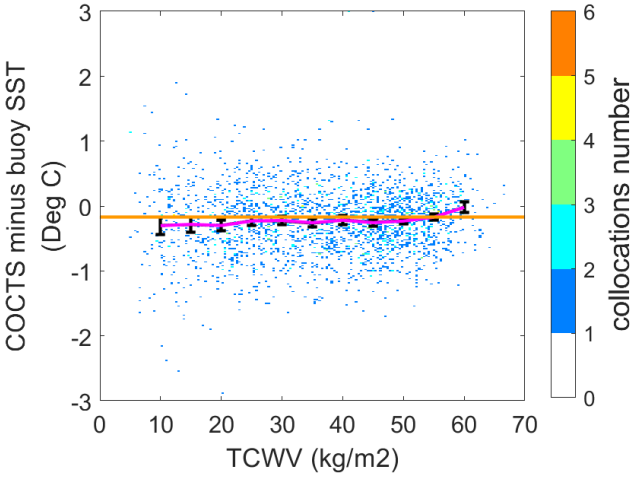

Fig. 11. The variations of COCTS minus buoy SST difference against TCWV. The background color represents the collocation numbers located in TCWV bin of 0.4 kg/m^2 and SST difference bin of 0.02 °C. The purple line is the variation of mean SST difference in every 5 kg/m^2 TCWV bin and the black bars represent the two times uncertainty in the mean. The orange horizontal line at −0.17 °C SST difference represent the cool skin effect.

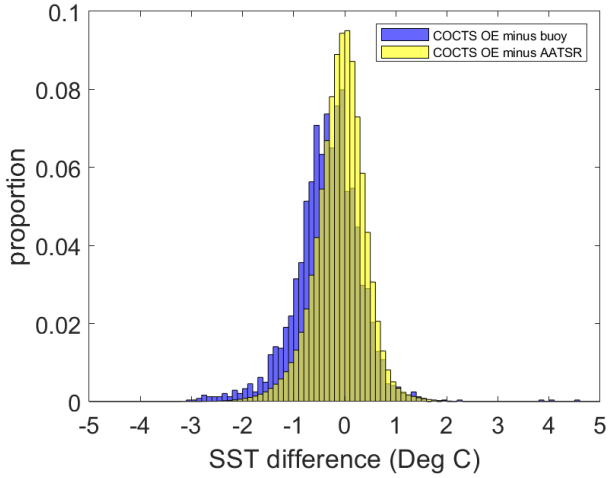

Fig. 12. The histograms of COCTS OE SST minus buoy SST difference (in blue bar) and COCTS OE SST minus AATSR SST difference (in yellow bar).

VI. Conclusion

In this research, the HY-1B COCTS SST is retrieved using the OE SST algorithm. Based on the unidirectional variational model, the de-striping of COCTS radiance is conducted. After de-striping, the striped noise in COCTS re-calibrated radiance is reduced significantly. Bayesian cloud detection algorithm is applied, and both the COCTS BT images and the retrieved SST validation distributions show that the cloud detection is effective for SST retrieval. The OE algorithm is used for COCTS SST retrieval, based on COCTS simulated BT and ERA Interim SST as the prior SST. The COCTS OE SSTs are compared with buoy SSTs and AATSR SSTs. The mean difference of COCTS minus buoy SST and COCTS minus AATSR SST are −0.23 ºC and −0.09 ºC, respectively, and the corresponding SDs are 0.51ºC and 0.49 ºC. Because of the series of sophisticated algorithms applied (cross-calibration, de-striping, Bayesian cloud detection and optimal estimation

© 2022 IEEE. Personal use is permitted, but republication/redistribution requires IEEE permission. See https://www.ieee.org/publications/rights/index.html for more information.

This article has been accepted for publication in IEEE Transactions on Geoscience and Remote Sensing. This is the author's version which has not been fully edited and content may change prior to final publication. Citation information: DOI 10.1109/TGRS.2022.3190444

retrieval), accuracy of COCTS OE SST is able to be equivalent to that of international high-quality SST products, with bias (as a skin SST) less than 0.1ºC and SD less than 0.5 ºC. The HY-1 series satellites are Chinese important marine satellites for ocean color and SST observations. The HY-1A and HY-1B satellites are experimental satellites, launched in 2004 and 2007, respectively. The HY-1C and HY-1D satellites are the operational satellites, launched in 2018 and 2020, respectively. In this paper, the de-striping, Bayesian cloud detection and optimal estimation SST retrieval algorithms worked well for HY-1B COCTS SST re-processing, therefor the SST accuracy of HY-1B COCTS improved a lot. This research also benefits development of cloud detection and SST retrieval of operational HY-1 series satellites, HY-1C and HY-1D satellites, since the algorithms used are suitable for operational implementation. It is also of great significance for the subsequent establishment of climate data record from HY-1 series satellites.

APPENDIX

This appendix provides computational details for the texture PDF applicable to COCTS cloud detection. Firstly, we estimate a PDF for the noise LSD of HY-1B COCTS according to its NEDT. Secondly, we derive the approximation relationship for the LSD of HY-1B COCTS, which we denote as y_{LSD}. For simplicity, we drop the subscript LSD. Specifically, y is estimated from the COCTS noise LSD, n ,and AATSR LSD, x, with negligible errors. It is formulated as the following equation (7),

$$y = \sqrt{n^2 + x^2} \tag{7}$$

where x, n, y are all positive real numbers. Thirdly, the distribution function of y can be formulated as the equation (8),

$$\begin{aligned} F_Y(y) = P(Y \le y) &= \iint_{\sqrt{n^2+x^2} \le y} f(n,x) dn dx \\ &= \int_{-\infty}^{\infty} \int_{-\infty}^{\sqrt{y^2-x^2}} f(n,x)\, dn dx \end{aligned} \tag{8}$$

We set $n = \sqrt{u^2 - x^2}$, where $u > x$ since $n > 0$, and then the integral can be reformulated as equation (9):

$$\int_{-\infty}^{\sqrt{y^2-x^2}} f(n,x)\, dn = \int_{-\infty}^{y} \frac{u}{\sqrt{u^2-x^2}} f\left(\sqrt{u^2-x^2}, x\right) du \tag{9}$$

.

Afterwards, we could obtain the distribution function $F_Y(y)$ as equation (10):

$$F_Y(y) = \int_{-\infty}^{y} \left[\int_{0}^{u-\epsilon} \frac{u}{\sqrt{u^2-x^2}} f_n\left(\sqrt{u^2-x^2}\right) f_x(x)\, dx \right] du \tag{10}$$

where ϵ is a small value to avoid numerical instability. Note that x and n are independent, and thus we can use their product to represent the joint PDF. We refer the integral item in square brackets [ ] as the convolution. It is worth noting that it follows a similar form of convolution, since the conventional convolution is $\int_{-\infty}^{\infty} f_n(u-x) f_x(x)\, dx$.

ACKNOWLEDGMENT

The authors would like to thank the anonymous reviewers for their constructive suggestions. HY-1B COCTS data were provided by NSOAS. The *in situ* SST data were provided by the iQuam System developed by the NOAA/ National Environmental Satellite, Data, and Information Service (NESDIS) STAR. The AATSR data were provided by ESA CCI project.

REFERENCES

[1] C. C. Walton, W. G. Pichel, and J. F. Sapper, "The development and operational application of nonlinear algorithms for the measurement of sea surface temperatures with the NOAA polar-orbiting environmental satellites," *J. Geophys. Res.*, vol. 103, no. C12, pp. 27999–28012, Nov. 1998, DOI: 10.1029/98JC02370.

[2] K. Saha, P. Dash, X. Zhao, and H. Zhang, "Error Estimation of Pathfinder Version 5.3 Level-3C SST Using Extended Triple Collocation Analysis," *Remote Sens.*, vol. 12, no. 4, pp. 590, Feb. 2020, DOI: 10.3390/rs12040590.

[3] K. A. Kilpatrick, G. Podestá, S. Walsh, E. Williams, V. Halliwell, M. Szczodrak, O.B. Brown, P.J. Minnett, and R. Evans, "A decade of sea surface temperature from MODIS," *Remote Sens. Environ.*, vol. 165, pp. 27–41, Aug. 2015, DOI: 10.1016/j.rse.2015.04.023.

[4] B. Petrenko, A. Ignatov, Y. Kihai, J. Stroup, and P. Dash, "Evaluation and selection of SST regression algorithms for JPSS VIIRS," *J. Geophys. Res. Atmos.*, vol. 119, no. 8, pp. 4580–4599, Apr. 2014, DOI: 10.1002/2013JD020637.

[5] C. J. Merchant, O. Embury, C. E. Bulgin, T. Block, G.K. Corlett, E. Fiedler, S.A. Good, J. Mittaz, N.A. Rayner, D. Berry, S. Eastwood, M. Taylor, Y. Tsushima, A. Waterfall, R. Wilson, C. Donlon, "Satellite-based time-series of sea-surface temperature since 1981 for climate applications," *Sci. Data*, vol. 6, pp. 223, Oct. 2019, DOI:10.1038/s41597-019-0236-x.

[6] O. Embury, C. J. Merchant, and G. K. Corlett, "A reprocessing for climate of sea surface temperature from the along-track scanning radiometers: Initial validation, accounting for skin and diurnal variability effects," *Remote Sens. Environ.*, vol. 116, pp. 62–78, Jan. 2012, DOI: 10.1016/j.rse.2011.02.028.

[7] B. Luo, P. J. Minnett, M. Szczodrak, K. Kilpatrick, and M. Izaguirre, "Validation of Sentinel-3A SLSTR derived Sea-Surface Skin Temperatures with those of the shipborne M-AERI," *Remote Sens. Environ.*, vol. 244, p. 111826, Jul. 2020, DOI: 10.1016/j.rse.2020.111826.

[8] N. Li, S. Wang, L. Guan, M. Liu, M. "Assessment of Global FY-3C/VIRR Sea Surface Temperature," *Remote Sens.*, vol. 13, no. 16, pp. 3249, Aug. 2021, DOI: 10.3390/rs13163249.

[9] P. J. Minnett, A. Alvera-Azcárate, T. M. Chin, G. K. Corlett, C. L. Gentemann, I. Karagali, X. Li, A. Marsouin, S. Marullo, E. Maturi, R. Santoleri, S. Saux Picart, M. Steele, and J. Vazquez-Cuervo, "Half a century of satellite remote sensing of sea-surface temperature," *Remote Sens. Environ.*, vol. 233, p. 111366, Nov. 2019, DOI: 10.1016/j.rse.2019.111366.

[10] K. A. Kilpatrick, G. P. Podestá, and R. Evans, "Overview of the NOAA/NASA advanced very high resolution radiometer Pathfinder algorithm for sea surface temperature and associated matchup database," *J. Geophys. Res.*, vol. 106, no. C5, pp. 9179–9198, May. 2001, DOI: 10.1029/1999JC000065.

[11] K. A. Kilpatrick, G. Podestá, E. Williams, S. Walsh, and P. J. Minnett, "Alternating decision trees for cloud masking in MODIS and VIIRS NASA sea surface temperature products," *J. Atmos. Ocean. Tech.*, vol. 36, no. 3, pp. 387–407, Mar. 2019, DOI: 10.1175/JTECH-D-18-0103.1.

[12] C. J. Merchant, C. Old, O. Embury, and S. MacCallum, "Generalized Bayesian cloud screening, Algorithm theoretical basis version 2.1", School of Geosciences, University of Edinburgh, Edinburgh, Scotland, Aug. 2008.

[13] C. J. Merchant, O. Embury, N. A. Rayner, D.I. Berry, G.K. Corlett, K. Lean, K.L. Veal, E.C. Kent, D.T. Llewellyn-Jones, J.J. Remedios, and R. Saunders, "A 20 year independent record of sea surface temperature for climate from Along-Track Scanning Radiometers," *J. Geophys.*

© 2022 IEEE. Personal use is permitted, but republication/redistribution requires IEEE permission. See https://www.ieee.org/publications/rights/index.html for more information.

This article has been accepted for publication in IEEE Transactions on Geoscience and Remote Sensing. This is the author's version which has not been fully edited and content may change prior to final publication. Citation information: DOI 10.1109/TGRS.2022.3190444

Res., vol. 117, no. C12, p. 12013, Dec. 2012, DOI: 10.1029/2012JC008400.

[14] C. E. Bulgin, J. P. D. Mittaz, O. Embury, S. Eastwood, and C.J. Merchant, "Bayesian Cloud Detection for 37 Years of Advanced Very High Resolution Radiometer (AVHRR) Global Area Coverage (GAC) Data," *Remote Sens.*, vol. 10, no. 2, p. 97, Jan. 2018, DOI: 10.3390/rs10010097.

[15] E. Maturi, A. Harris, C. Merchant, J. Mittaz, and J. Sapper, "NOAA's Sea Surface Temperature Products From Operational Geostationary Satellites," *Bull. Am. Meteorol. Soc.*, vol. 89, no. 12, pp. 1877–1888, Dec. 2008, DOI: 10.1175/2008BAMS2528.1.

[16] Y. Kurihara, H. Murakami, and M. Kachi, "Sea surface temperature from the new Japanese geostationary meteorological Himawari‐8 satellite, *Geophys. Res. Lett.*, vol. 43, no. 3, pp. 1234–1240, Jan. 2016, DOI: 10.1002/2015GL067159.

[17] M. L. McMillin, "Estimation of sea surface temperatures from two infrared window measurements with different absorption," *J. Geophys. Res.*, vol. 80, no. 36, pp. 5113–5117, Dec. 1975, DOI: 10.1029/JC080i036p05113.

[18] E. P. McClain, W. G. Pichel, and C. C. Walton, "Comparative performance of AVHRR-based multichannel sea surface temperatures," *J. Geophys. Res.*, vol. 90, no. C6, pp. 11587–11601, Nov. 1985, DOI: 10.1029/JC090iC06p11587.

[19] D. T. Llewellyn-Jones, P. J. Minnett, R. W. Saunders, and A. M. Zavody, "Satellite multichannel infrared measurements of sea surface temperature of the N.E. Atlantic Ocean using AVHRR/2," *Quarr. J. R. Met. Soc*., vol. 110, no. 465, pp. 613-631, 1984, DOI: 10. 1002/qj.49711046504

[20] C. J. Merchant, A. R. Harris, M. J. Murray, and A. M. Závody, "Toward the elimination of bias in satellite retrievals of sea surface temperature: 1. Theory, modeling and interalgorithm comparison," *J. Geophys. Res.*, vol. 104, no. C10, pp. 23565–23578, Oct. 1999, DOI: 10.1029/1999JC900105.

[21] C. J. Merchant and P. L. Borgne, "Retrieval of Sea Surface Temperature from Space, Based on Modeling of Infrared Radiative Transfer: Capabilities and Limitations," *J. Atmos. Ocean. Tech.*, vol. 21, no. 11, pp. 1734–1746, Nov. 2004, DOI: 10.1175/JTECH1667.1.

[22] C. J. Merchant, D. Llewellyn-Jones, R.W. Saunders, N. A. Rayner, E. C. Kent, C. P.Old, D. Berry, A. R. Birks, T. Blackmore, G. K. Corlett, O. Embury, V. L. Jay, J. Kennedy, C.T. Mutlow, T. J. Nightingale, A. G. O'Carroll, M.J. Pritchard, J. J. Remedios, and S. Tett, "Deriving a sea surface temperature record suitable for climate change research from the along-track scanning radiometers," *Adv. Space Res.*, vol. 41, no. 1, pp. 1–11, 2008, DOI: 10.1016/j.asr.2007.07.041.

[23] L. M. McMillin and D. S. Crosby, "Theory and validation of the multiple window sea surface temperature technique," *J. Geophys. Res.*, vol. 89, no. C3, pp. 3655–3661, May. 1984, DOI: 10.1029/JC089iC03p03655.

[24] C. J. Merchant, P. L. Borgne, A. Marsouin, and H. Roquet, "Optimal estimation of sea surface temperature from split-window observations," *Remote Sens. Environ.*, vol. 112, no. 5, pp. 2469–2484, May. 2008, DOI: 10.1016/j.rse.2007.11.011.

[25] C. J. Merchant, P. L. Borgne, H. Roquet, and A. Marsouin, "Sea surface temperature from a geostationary satellite by optimal estimation," *Remote Sens. Environ.*, vol. 113, no. 2, pp. 445–457, Feb. 2009, DOI: 10.1016/j.rse.2008.10.012.

[26] C. J. Merchant, P. L. Borgne, H. Roquet, and G. Legendre, "Extended optimal estimation techniques for sea surface temperature from the Spinning Enhanced Visible and Infra-Red Imager (SEVIRI)," *Remote Sens. Environ.*, vol. 131, pp. 287–297, Apr. 2013, DOI: 10.1016/j.rse.2012.12.019.

[27] M. Liu, C. J. Merchant, L. Guan, and J. P. Mittaz, "Inter-Calibration of HY-1B/COCTS Thermal Infrared Channels with MetOp-A/IASI," *Remote Sens.*, vol. 10, no. 8, p. 1173, Jul. 2018, DOI: 10.3390/rs10081173.

[28] M. Bouali and A. Ignatov, "Estimation of Detector Biases in MODIS Thermal Emissive Bands," *IEEE Trans. Geosci. Remote Sens.*, vol. 51, no. 7, pp. 4339–4348, Jul. 2013, DOI: 10.1109/TGRS.2012.2230183.

[29] P. Berrisford, D. P. Dee, P. Poli, R. Brugge, M. Fielding, M. Fuentes, P.W. Kållberg, S. Kobayashi, S. Uppala, and A. Simmons, "The ERA-Interim archive, version 2.0," ECMWF, Shinfield Park, Reading, UK, Nov. 2011.

[30] D. P. Dee et al., "The ERA‐Interim reanalysis: configuration and performance of the data assimilation system," *Q. J. Roy. Meteor. Soc.*, vol. 137, no. 656, pp. 553-597, Apr. 2011, DOI: 10.1002/qj.828.

[31] C. Bulgin, SST CCI Auxiliary Datasets, 2019, DOI: 10.5281/zenodo.2586714.

[32] C. Merchant, "Comparisons of radiative transfer simulations for SEVIRI (thermal channels)", visiting scientist report, July-October, 2003.

[33] C. J. Merchant, A. R. Harris, H. Roquet, and P. L. Borgne, "Retrieval characteristics of non-linear sea surface temperature from the Advanced Very High Resolution Radiometer," *Geophys. Res. Lett.*, vol. 36, no. 17, pp. 1397–1413, Sep. 2009, DOI: 10.1029/2009GL039843.

[34] C. D. Rodgers, "Inverse Methods for Atmospheric Sounding: Theory and Practice", World Scientific Publishing, Singapore, 2000.

[35] F. Xu and A. Ignatov, "Error characterization in iQuam SSTs using triple collocations with satellite measurements", *Geophys. Res. Lett.*, vol. 43, no. 20, pp. 10,826-10,834, Oct. 2016, DOI: 10.1002/2016GL070287.

[36] C. J. Donlon, P. J. Minnett, C. Gentemann, T. J. Nightingale, I. J. Bartom, B. Ward, M. J. Murray, "Toward Improved Validation of Satellite Sea Surface Skin Temperature Measurements for Climate Research," *J. Climate*, vol. 14, no. 4, pp. 353–369, Feb. 2002, DOI: 10.1175/1520-0442(2002)015<0353:TIVOSS>2.0.CO;2.

Mingkun Liu (M'15) received the B.S. degree in Marine Technology from Ocean University of China, Qingdao, China, in 2014, and Ph.D. degree in Marine Detection Technology from Ocean University of China, Qingdao, China in 2019. She visited University of Reading in UK and conducted research on infrared sea surface temperature from September 2017 to September 2018.

She has been working on research and teaching at Ocean University of China since graduation. Her research interests are validation and retrieval of sea surface temperature from satellite infrared and microwave radiometers. She teaches undergraduate courses on College Physics.

Christopher J. Merchant received a 1st in Physics from University of Oxford (1989) and, after a period working in industry, a Ph.D. in Space and Climate Physics from University College London (1999). He joined the University of Edinburgh as a lecturer in the department of meteorology, and since 2013 has been Professor of Ocean and Earth Observation at University of Reading, UK.

His research interests focus on thermal remote sensing for climate applications, and he has authored and co-authored more than 120 journal articles.

Owen Embury received the B.A. degree in physics from University of Cambridge, UK in 2001, and the MSc. and Ph.D. in remote sensing from University of Edinburgh, UK in 2004 and 2013 respectively.

From 2004 to 2013, he was a Research Associate with the University of Edinburgh. Since 2013, he has been a Research Assistant with the University of Reading, UK. His research

© 2022 IEEE. Personal use is permitted, but republication/redistribution requires IEEE permission. See https://www.ieee.org/publications/rights/index.html for more information.

This article has been accepted for publication in IEEE Transactions on Geoscience and Remote Sensing. This is the author's version which has not been fully edited and content may change prior to final publication. Citation information: DOI 10.1109/TGRS.2022.3190444

interests include satellite remote sensing, primarily accurate estimates of sea surface temperature and cloud detection from infrared instruments.

Jianqiang Liu received a B.S. degree in geophysics from Peking University, Beijing, China, in 1986 and a Master's degree in marine meteorology from National Marine Environmental Forecasting Center, State Oceanic Administration, Beijing, China in 1989.

He is the chief designer of the ground application system for Chinese-France Ocean satellite and new generational ocean color satellites, and was a deputy chief designer of the ground application system for HY-1 and HY-2 satellites. He is one of the founders of satellite ocean remote sensing in China and plays an important role in the development of Chinese ocean satellite and manned space flight. His research interests include ocean color and sea wave satellite data processing, applications of ocean remote sensing data and Antarctic research.

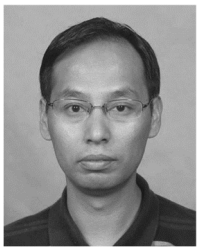

Qingjun Song received the B.S. degree in applied physics from the Hefei University of Technology, Hefei, China, in 2001 and the M.S. degree in ocean technology from Dalian Ocean University, Dalian, China, in 2012.

He is currently a Researcher with the National Satellite Ocean Application Service, Ministry of Natural Resources, Beijing, China, currently working on HY1 and HY2 series satellite instrument calibration and ocean remote sensing product validation. His research interests include remote sensing, the absolute radiometric calibration of optical instruments.

Lei Guan (M'05) received the B.S. degree in Electronic Engineering from Ocean University of Qingdao, Qingdao, China, in 1992 and Ph.D. degree in Marine Physics from Ocean University of Qingdao in 1998.

She has been working on research and teaching at Ocean University of China (formerly Ocean University of Qingdao) since graduation. She is a Professor in the College of Marine Technology, Faculty of Information Science and Engineering/Sanya Oceanographic Institution, Ocean University of China. She visited Tohoku University in Japan and conducted research there from September 2000 to September 2001. Her research interests include remote sensing of the oceanic parameters, primarily in the retrieval, validation and merging of multi-sensor sea surface temperature. She has been principal investigator for the national projects related with SST studies and involved in the international projects such as EC FP6 DRAGONESS project, China/ESA Dragon project, IOC/WESTPAC New Generation SST project. She has been a member of the Group for High Resolution Sea Surface Temperature (GHRSST) Science Teams since 2011. She advises graduate students and teaches undergraduate and graduate courses on Digital Image Processing, Introduction to Atmospheric Science, Atmospheric Radiative Transfer, IDL Programming for Satellite Data Processing.

© 2022 IEEE. Personal use is permitted, but republication/redistribution requires IEEE permission. See https://www.ieee.org/publications/rights/index.html for more information.